Guest Editorial
An Overview of the Seabed Characterization Experiment

IN LITTORAL ocean environments, knowledge of the acoustic properties of the seabed is generally required to predict the acoustic field. An ability to make accurate predictions of the acoustic field is important in the areas of sonar, acoustic communication, and navigation. Much effort has been expended over the past half-century to understand and model the acoustic behavior of sandy sediments, composed primarily of medium or coarse grains, over the entire frequency range of interest to underwater acoustics, $\mathcal{O}(10)$ Hz to $\mathcal{O}(1)$ MHz. Extensive measurements of sound speed and attenuation in sandy sediments have been collected over large portions of the world and compared to models [see, for example, item 1) of the Appendix], but such is not the case for fine-grained sediments. The work described in this special issue seeks to address this deficiency.

Seabed Characterization Experiment (SBCEX) was an international, multidisciplinary, and multi-institutional research project devoted to the following scientific goals:

1) to understand the physical mechanisms that control acoustic propagation in fine-grained sediments;
2) to quantify uncertainties in the estimation of seabed parameters;
3) to correlate the observed horizontal variations in the acoustical field with the measured horizontal variability of the seabed;
4) to assess the performance of the resulting geoacoustic models, inversions, and statistical inference methods.

To facilitate these scientific goals, the experiment was designed to minimize complexity in both the water column and the seabed. Referring to the prediction of acoustic fields in shallow water waveguides, the general goal of the experiment was to identify remote sensing techniques that could provide the necessary acoustic characterization of the seabed, that in turn would provide accurate prediction of the acoustic field in the 10 Hz to 10 kHz band.

The present special issue contains 15 papers related to SBCEX. In this guest editorial, we first provide the broad context for the experiment in comparison to a number of other recent large-scale field experiments. Next, a summary of the participants and their measurements is provided. Finally, we collect, compare, and discuss all of the sound-speed measurements and inferences contained in the papers in this special issue. This represents the initial collection of reporting from SBCEX and a second volume of this special issue is forthcoming.

The site of the experiment, shown in Fig. 1, is in approximately 75 m of water, about 95 km south of Martha's Vineyard, MA, USA, in an area historically known as the New England Mud Patch. However, the results of the present project indicate that the sediment is not composed of pure mud, but rather contains various proportions of silt, clay, and sand. For simplicity, within this editorial, the upper layer of sediment within the experimental site is referred to as mud. The aforementioned goal of environmental simplicity was largely achieved. The water column was stable and nearly isothermal during the acoustic experiments in the late winter and early spring of 2017. Also, the bottom was essentially flat and the center of the site contained up to about 12 m of a fine-grained sediment with a comparatively small amount of coarser grained material.

The international, multidisciplinary, and multi-institutional research team collected a large and diverse data set. Two survey cruises conducted in 2015 and 2016 performed detailed subbottom profiling and collected more than 200 sediment cores. In 2017, a series of experiments took place primarily during March and April: Three research vessels (RVs) and more than a dozen principle investigators conducted several types of experiments, including impulsive and tonal source tows received on vertical and horizontal line arrays (VLAs and HLAs), and direct measurements of sediment bulk acoustic waves and interface waves. A list of participating institutes is given in Table I along with the principle points of contact. Acronyms for the institutes, which will be used throughout this overview, are also provided in Table I.

I. Brief Comparison of SBCEX to Recent Large-Scale Field Experiments

In this section, we illustrate some of the differences between SBCEX and other recent large-scale field experiments that studied the acoustics of the seabed, specifically the Asian Seas International Acoustics Experiments of 2000 and 2001, the Sediment Acoustics Experiments of 1999 and 2004, and Shallow Water 2006. The present work has benefitted from and was informed by the work preceded it.

A. ASIAEX

The Asian Seas International Acoustics Experiment (ASIAEX) was conducted in the East China Sea (ECS) and South

Digital Object Identifier 10.1109/JOE.2019.2956606

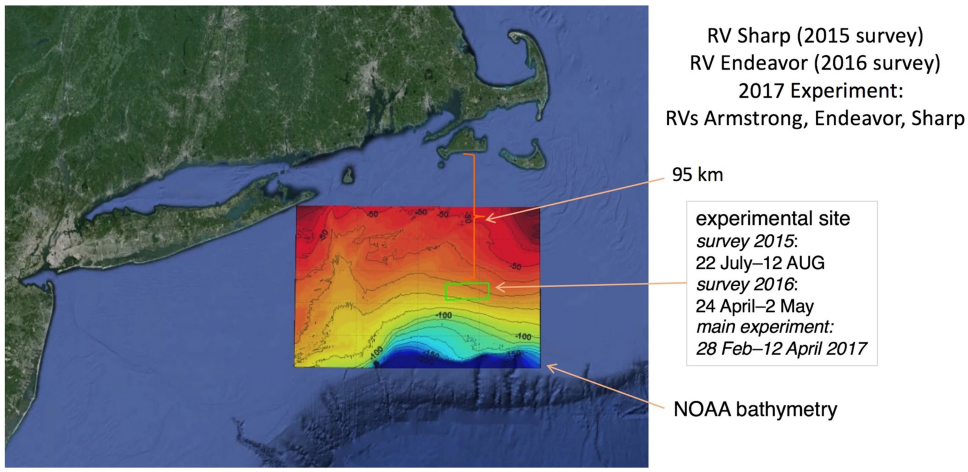

Fig. 1. Site of the SBCEX is south of the southern New England coast. The vessels that participated in various phases of the experiment are shown, along with the dates of the operations. NOAA bathymetry (10-m isobaths) is also shown. The experimental site itself was within the green rectangle.

TABLE I
LIST OF PARTICIPATING INSTITUTIONS AND ASSOCIATED POINTS OF CONTACT

Acronym	Institute	Points of Contact
APL-UW	Appl. Physics Lab. Univ. of Washington	Peter Dahl and Jie Yang
ARL:PSU	Appl. Res. Lab, The Pennsylvania State Univ.	Charles Holland and Chad Smith
ARL:UT	Appl. Res. Labs, The Univ. of Texas at Austin	Preston Wilson
CMRE	Centre for Maritime Research and Experimentation	Yong-Min Jiang
FFI	Forsvarets forskningsinstitutt, Norway	Dag Tollefsen
KSA	Knobles Scientific and Analysis, LLC	David Knobles
MPL	Marine Physical Laboratory, Scripps Inst. of Oceanog.	William Hodgkiss
NRL	Naval Research Laboratory	Allen Reed[1]
NUS	National University of Singapore	Venugopalan Pallayil
UD	Univ. of Delaware	Mohsen Badiey and Lin Wan
URI	Univ. of Rhode Island	Jim Miller and Gopu Potty
USGS	United States Geographic Survey	Jason Chaytor
UTIG	Inst. for Geophysics, The Univ. of Texas at Austin	John Goff
WHOI	Woods Hole Oceanographic Institute	Ying-Tsong Lin

[1]Present affiliation: Naval Oceanographic Office.

China Sea (SCS) in 2000 and 2001 and bears the most similarity to SBCEX. The SCS effort was focused on the acoustic effects of water column variability [item 2) of the Appendix]; however, the ECS effort included a component on seabed acoustics. The goals of the ECS effort were: first, to identify and elucidate properties of shallow-water boundaries governing propagation and reverberation in the ECS, such as sediment inhomogeneity, sediment roughness, and sea surface roughness; and second, to establish a geoacoustic description for the ECS seabed, based on complementary approaches to inverting acoustic propagation and reverberation measurements made in the $\mathcal{O}(10^1$–$10^4)$ Hz frequency range [item 3) of the Appendix].

SBCEX differs from ASIAEX in several key ways.

1) SBCEX had an increased focus on the seabed. All of the acoustic measurements in SBCEX were focused on some form of acoustic interaction with the seabed.
2) SBCEX had an increased mean spatial resolution of direct sediment sampling (area of site divided by total number of cores). In SBCEX, more than 200 cores were collected using gravity, piston, vibracore, and multicore tools. This number is more than three times the 60 cores collected in ASIAEX, corresponding to a difference of 250 km^2 per core in ASIAEX, versus about 1.65 km^2 per core in SBCEX.
3) The SBCEX site had finer grained sediment and more uniform sediment properties than the ASIAEX ECS site. Both experiments deployed small explosive charges in

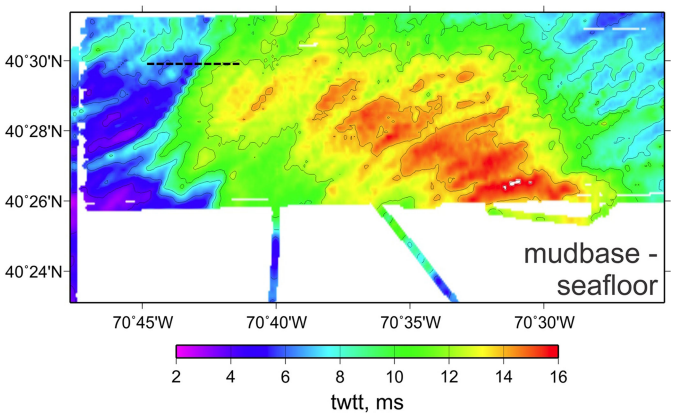

Fig. 2. Closeup of the area around the green rectangle from Fig. 1. The color map indicates the thickness of the surficial mud layer (an isopach map) in units of two-way acoustic travel time (milliseconds). Assuming a sound speed of 1500 m/s, the thickest part of the mud is approximately 12 m. The black dashed line indicates the location of the survey line shown in Fig. 3. Figure courtesy of John Goff.

circles around arrays. Within the ECS circle, the upper layer was a thin veneer about 1 m thick [item 3) of the Appendix]. Within the SBCEX circle, the upper layer ranged from about 9–12 m thick [item 4) of the Appendix]. Within the SBCEX circle, the sediment was of a uniform mean grain type (silt.)[1] and more fine grained, with a mean grain size of 6.33φ (medium silt) and a range of $4.9 < \varphi < 7.2$ (coarse silt to very fine silt), in the upper 200 cm of sediment [item 4) of the Appendix], where φ is the Krumbein phi scale [item 6) of the Appendix]. The ASIAEX ECS circle had sandy sediments ($\varphi < 4.3$) to the east and silty sediments to the west ($\varphi > 4.3$), with a grain size range of $3.7 < \varphi < 5.8$ (very fine sand to medium silt) [item 7) of the Appendix]. The ECS fractional porosity ranged from about 0.35 to about 0.55 [item 8) of the Appendix], and in SBCEX, the fractional porosity ranged from about 0.52 to 0.65 [item 4) of the Appendix].

4) SBCEX deployed two forms of direct sound-speed measurement in the sediment [items 9) and 10) of the Appendix], in addition to sound speeds derived from core logger measurements [items 9), 11), and 12) of the Appendix]. ASIAEX ECS had only core logger derived sound speeds [item 7) of the Appendix].
5) Both ASIAEX ECS and SBCEX utilized small explosive charges (38 and 31 g, respectively, [item 3) and 13) of the Appendix]), but SBCEX also utilized a number of deterministic sources as shown in Table II.
6) The late winter season was chosen for SBCEX specifically to provide a stable water column with near-isovelocity conditions throughout the site. An example is given in Fig. 2 of item 14) of the Appendix, which shows a typical variation of about 1 m/s in depth (due primarily to pressure) and about 1.5-m/s variation across eight days. In comparison, there was nearly a 10-m/s sound-speed variation with depth in ASIAEX ECS, and as much as 7.5-m/s variation over 24 h, as shown in Fig. 4 of item 3) of the Appendix.

[1]The size classification used here follows the Wentworth scale [item 5) of the Appendix].

TABLE II
ACOUSTIC SOURCES DEPLOYED DURING SBCEX2017

Acoustic Sources	PI	Institute
AA201 boomer	Holland	ARL:PSU
CSS	Wilson	ARL:UT
iWaSP	Potty/Miller	URI
ITC-2015	Hodgkiss	MPL
J15-1	Hodgkiss	MPL
J15-1	Dahl/Dall'Osto	APL-UW
LFM and CW	Badiey/Wan	UD
M18-C	Holland/Smith	ARL:PSU
Moored and AUV sources	Lin	WHOI
SUS	Wilson/Knobles/Schoch	ARL:UT/KSA/NUWC

TABLE III
RECEIVING ARRAYS AND SYSTEMS DEPLOYED DURING SBCEX17

Arrays/Systems	PI	Institute
Acoustic Gliders	Jiang	NATO CMRE
ACS	Ballard *et al.*	ARL:UT
ARLUT L array	Wilson	ARL:UT
AUV-DTLA	Pallayil/Lin	NUS-ARL/WHOI
Multi-sensor Core Logger	Reed	NRL
Deep Sound	Buckingham	MPL
FFI HLA	Tollefsen	FFI Norway
FORA	Holland/Smith	ARL:PSU
Geosled	Potty/Miller	URI
IVAR	Dahl/Dall'Osto	APL-UW
IWASP	Potty/Miller	URI
MPL VLA 1	Hodgkiss	MPL
MPL VLA 2	Hodgkiss	MPL
Reflection hyd string (RHS)	Holland	ARL:PSU
SAMS	Yang	APL-UW
SHRU	Lin	WHOI
UD VLA	Badiey/Wan	UD

B. *SAX99 and SAX04*

The Sediment Acoustics Experiments conducted in 1999 and 2004 (SAX99 and SAX04, respectively) were focused on sandy sediments and direct measurement techniques and modeling, and included significant efforts to study penetration into, propagation within and scattering from the seabed, in the presence of ripples and bioturbation. Significant physical characterization of the sediment material was also conducted. Hurricane Ivan swept through the experimental area during the 2004 experiment, mixing the sediment significantly compared to the 1999 experiment.

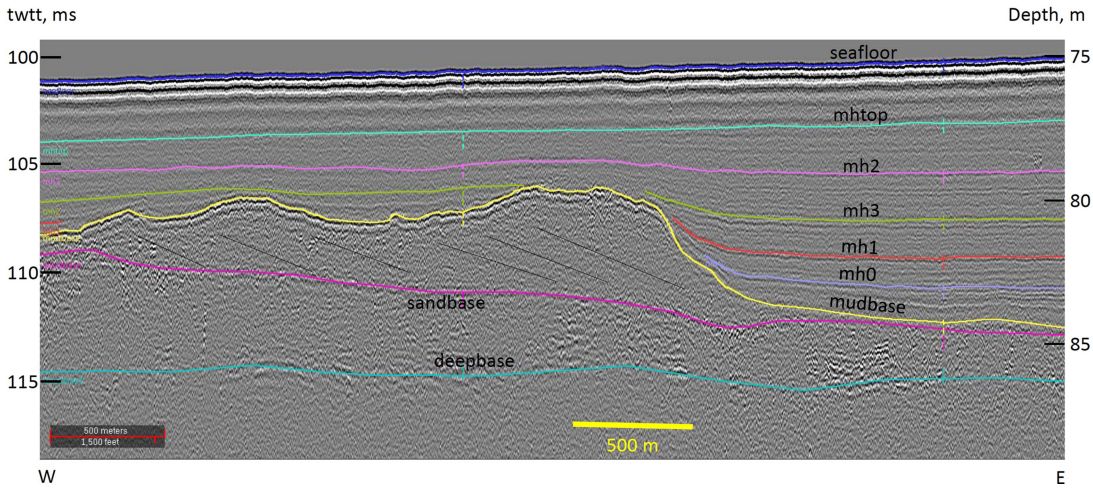

Fig. 3. Interpreted full-waveform chirp record from the survey line indicated in Fig. 2. The mud layer lies between the seafloor and the mud base. A layer of sand lies below, followed by a deeper base unit. Interpretation and figure courtesy of John Goff, adapted from item 27) of the Appendix. Conversion of TWTT to depth assumes a sound speed of 1500 m/s. The yellow horizontal length bar represents 500 m.

Overviews of the SAX experiments are provided in three special issue editorials on the topic [items 15)–17) of the Appendix].

The major differences between SBCEX and the SAX experiments are sediment composition and the relative importance of direct measurements and inferences. The sandy sediments in SAX99 and SAX04 were composed of significantly larger grain sizes than in SBCEX. The mean grain size in SAX99 was 1.27φ (medium-grained sand) assessed via 27 diver cores at a mean spatial resolution of 0.3 km^2 per core, and to a depth of about 22 cm [item 18) of the Appendix]. Fractional porosity varied from 0.35 to 0.40 in the cores. In SAX04, core sampling resolution was similar. The mean grain size was 1.47φ (medium sand) and mean fractional porosity was 0.36, not significantly different than in SAX99 [item 19) of the Appendix].

One of the outcomes of the SAX experiments that SBCEX sought to replicate was the wideband sound speed and attenuation results that were collected and compared to theory [see, for example, Figs. 3 and 4 in item 20) of the Appendix from SAX99 and Fig. 18 of item 21) of the Appendix from SAX04]. At the time of conception of SBCEX, nothing comparable was present in the literature for fine-grained sediments. Hence, a goal of SBCEX was to bridge the gap in the body of knowledge reported in the literature between the very low frequency regime ($\ll$1 kHz) and the mid-frequency regime (1–10 kHz). That goal has been partially addressed in this special issue, as described below.

C. SW06

Shallow Water 2006 (SW06) took place during July–September of 2006 and was conducted near the 80-m isobath on the continental shelf off Atlantic City, NJ, USA. Its goal was to study in detail the impact of various dynamic environmental processes on sound propagation. An overview of SW06 is given in item 22) of the Appendix and in the guest editorials of three special issues that contain papers reporting results from the experiment [items 23)–25) of the Appendix]. It was an extensive operation that included seven ships, 62 acoustic and oceanographic moorings, aircraft overflights, satellite coverage, ten oceanographic gliders, and dozens of principal investigators [item 23) of the Appendix]. One key difference is the dynamic water column during SW06. Whereas a stable water column was sought for SBCEX and was present during the SBCEX 2017 experiment, the site and time-of-year for SW06 selected to ensure shelf break fronts and internal waves were present during the acoustic experiments. In SBCEX a comparatively simple site geology was sought and found, compared to a more complicated site geology in SW06.

One of the thrusts of SW06 was the effect of water column variability on sound propagation, but several efforts leading up to and during SW06 included direct measurements of sediment acoustic properties and the estimation of sediment acoustic properties via inference and inversion techniques. Extensive bottom sampling was also conducted. In total, 98 grab samples and 18 short cores were collected and analyzed for grain size and porosity just before SW06, augmenting a long history of environmental characterization at that site, including swath bathymetry, seismic profiling, sidescan surveys, and coring. *In situ* sound-speed measurements at 65 kHz were also obtained at the SW06 site before the main experiment. These measurements, analyses, and historical environmental characterization efforts were reviewed in item 26) of the Appendix. The new seabed sampling reported in item 26) of the Appendix occurred at a mean spatial resolution of 12.9 km^2 per sample. The mean grain size over the entire set of samples and cores was 1.61φ and there was significant spatial variability of the weight fraction of fine ($\varphi > 4$) and coarse grains ($\varphi < -2$) contained in the samples. The range of fine weight fractions varied from 0.6% to 20.1%, and the range of coarse weight fractions varied from 0.6% to 8.6%. Fractional porosity was reported for a subset of the samples and it ranged from 0.39 to 0.55.

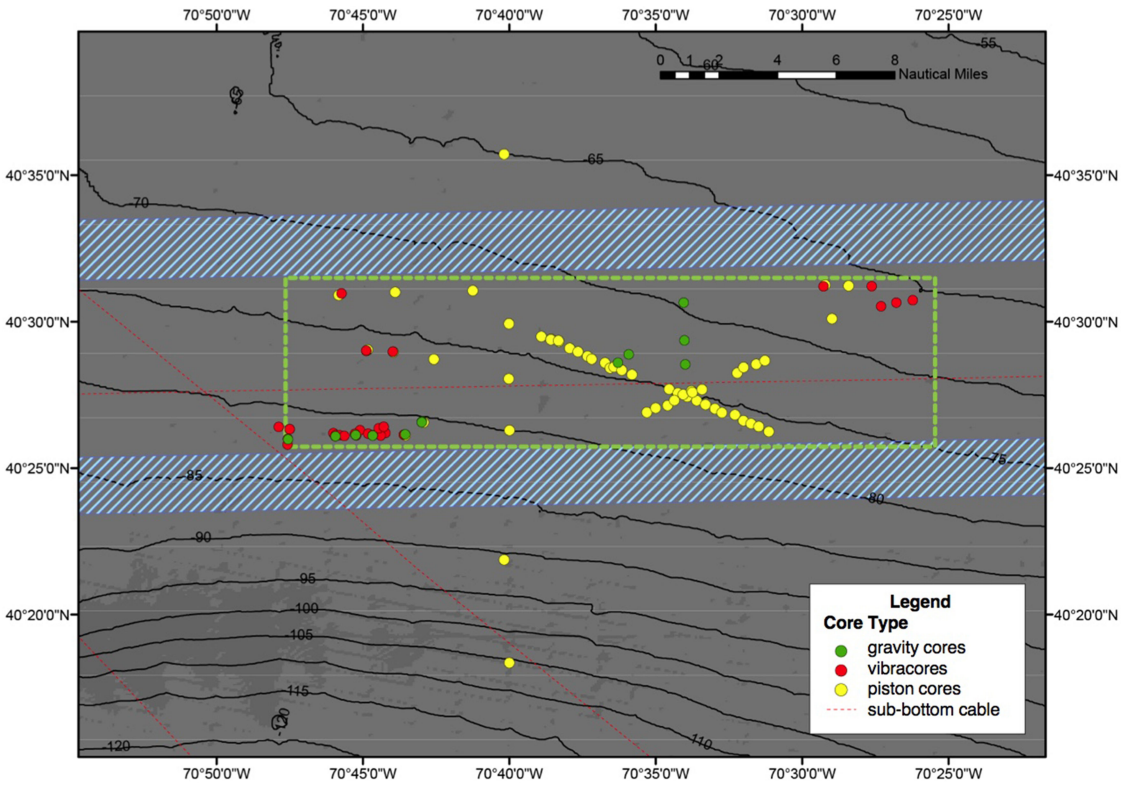

Fig. 4. Locations of the piston core sites (yellow circles, obtained by Jason Chaytor USGS), the vibracore sites (red circles, obtained by John Goff UTIG), and acoustic gravity core sites (green circles, obtained by Ballard *et al.* ARL:UT) from the 2016 survey. Bathymetry contours are shown with black lines. The locations of inbound and outbound New York City shipping lanes are shown with the blue cross hatch markings, directly north and south of the experimental site. Figure courtesy of Jason Chaytor.

To summarize, the following are unique characteristics of SBCEX:

1) a focus on direct and inverse assessments of the acoustic properties of *fine-grained* sediments;
2) a comparatively flat site bathymetry;
3) a stable, nearly isothermal, isovelocity sound-speed profile during the 2017 experiment;
4) an extensive region with a comparatively thick and comparatively uniform upper layer of fine-grained sediment;
5) dedicated and extensive coring;
6) dedicated and extensive subbottom profiling and multibeam bathymetry surveys.

II. Surveys 2015 and 2016: Mud Thickness Map and Sediment Cores

One of the primary outputs of the 2015 survey was a mud thickness map (isopach map), shown in Fig. 2, in units of two-way travel time (TWTT), produced by Goff *et al.* using a subbottom chirp profiler towed behind *RV Hugh R. Sharp* in July 2015 [item 27) of the Appendix]. Several other layers are present, as is indicated in Fig. 3, which is a portion of a single E-W survey line at about 40° 30′ N (the dashed line in Fig. 2).

The data set from which Figs. 2 and 3 were derived represents a spatial acoustic record of the subbottom that assisted researchers in setting the bounds on geoacoustic models of the site. The core samples taken during the 2015 and 2016 surveys provide a link to the physical nature of the sediments in those layers. Fig. 4 shows a map of the experimental site that includes the locations where cores were obtained in the 2016 survey cruise. The 25 sites of the core sampling in 2015 are not shown to save space, but complement the 2016 core sites. For the 2016 coring, 53 successful piston cores targeting mud units were obtained, but they also sampled significant sand in some locations, and 25 successful vibracores targeting thin mud regions to sample sands beneath were obtained. For the 2016 cores, multisensor core logging (MSCL) was conducted by Allen Reed on the ship,[2] between 2 and 4 h after recovery, once the cores came to thermal equilibrium [items 9), 11), and 12) of the Appendix]. The core logging provided measurements of density and high frequency (250 kHz) sound speed as a function of length along the cores, to complement the TWTT chirp survey records. An acoustic measurement system was also deployed at the end of a gravity corer, by Ballard *et al.*, during the 2016 survey, which yielded direct *in situ* measurements of sound speed (25–200 kHz) at locations indicated by the green circles in Fig. 4 [item 9) of the Appendix]. While these measurements provide some prior knowledge for inverse and statistical inference analyses, they

[2]The core logging from the 2015 survey was done on shore after the cruise due to failure of the core logging equipment during the cruise.

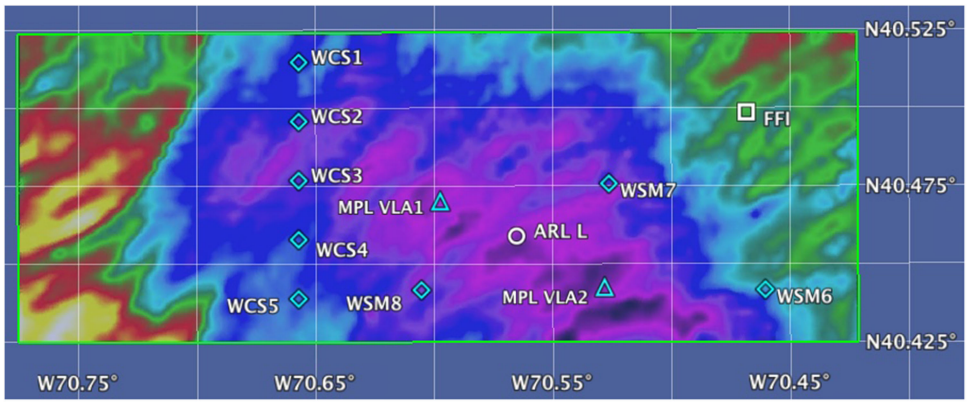

Fig. 5. Locations of the environmental and acoustic moorings deployed in the main experiment are superimposed over the mud thickness map: eight oceanographic moorings (labels that begin with "W"), moorings WCS1, 3, and 5 included an acoustic Doppler current profiler, WCS2 included a low-frequency source, WCS4 included a single hydrophone recording unit, and WSM6, 7, and 8 each included a low-frequency source. Scripps MPL deployed two vertical line arrays (VLA). ARL:UT deployed an L-array. FFI deployed an HLA. UD also deployed a VLA (not shown) very close to the ARL:UT array.

do not provide ground truth, due in part to the difference in the frequency ranges used during the surveys and the frequency range of the acoustic measurements in the main experiment, and in part due to the disturbance of the natural state of the sediments caused by the direct sampling.

In addition, oceanographic measurements, shipboard CTD casts, shipboard laboratory sediment acoustics measurements made using box and gravity core samples, photographic ocean bottom imagery, sediment infauna collection and assessment, bottom water collection, and some preliminary acoustic propagation measurements were also conducted during the two survey cruises. Finally, a multibeam bathymetry survey was conducted during the 2015 survey cruise, by de Moustier [item 28) of the Appendix] with subsequent additional data processing conducted by Goff [item 29) of the Appendix].

III. Main Experiment: February–April 2017

The main experiment was focused on sound propagation measurements using both impulsive and tonal sources (see Tables II and III). Supporting oceanographic measurements were obtained to provide the necessary water column environmental model inputs. The sediment acoustic measurement system (SAMS) was deployed by Yang *et al.* to directly measure sediment sound speed [item 10) of the Appendix]. The source, receiver, and oceanographic moorings deployed during the 2017 experiment are shown in Fig. 5 and described briefly in the accompanying caption. Much of the work conducted during the 2017 experiment is described in this special issue and is summarized in Section V.

IV. Special Issue Summaries

Provided below is a brief summary of each paper in this special issue. The papers are divided into four categories: source modeling, direct measurements, short-range remote sensing, and long-range remote sensing. The work described below occurred during the 2017 experiment, unless stated otherwise.

A. Source Modeling

Wilson *et al.* [item 13) of the Appendix] report on one of impulsive sources used in SBCEX. U.S. Navy Signal Underwater Source (SUS) Mk 64 charges, which contained 31.18 g of the explosive tetryl, were deployed to generate wideband signals and were utilized in a variety of inversion analyses. Source recordings were obtained by two hydrophones deployed from the source ship and were analyzed for bubble period, energy spectral density, and the variability of these parameters. Measured parameters were compared to previous results from the literature as well as predictions of a new semiempirical time-domain model. The new model describes the source-level measurements in the 25–275-Hz band and in the 400-Hz octave band to within 0.5 dB, and agrees with similar measurements from the literature to within 0.6 dB. The standard deviation of the band-limited source levels was found to be about 1 dB, some of which is ascribed to uncertainty and variation in the source-to-receiver distance. The observed source-level variation is similar to previously reported values.

B. Direct Measurements

Ballard *et al.* [item 9) of the Appendix] present *in situ* measurements of sediment sound-speed profiles using the acoustic coring system (ACS) during the 2016 survey cruise. The measurements were obtained from seven gravity cores collected in the New England Mud Patch. The ACS uses two sets of transducers mounted below the penetrating tip of a sediment corer to make sound-speed measurements using pulsed sinusoids as the corer penetrates the seabed. The *in situ* sound-speed profiles were interpreted in the context of stratigraphic layering measured by the chirp survey and were compared to the sound-speed measurements at 250 kHz from Reed's MSCL. Using porosity and grain size distributions measured from discrete samples of the cored sediments, the *in situ* sound-speed measurements were compared to empirical regressions based on independent data sets.

Yang and Jackson [item 10) of the Appendix] present direct simultaneous measurements of the sediment sound speed over the surficial 3 m of sediments measured by the SAMS at 18 sites in the 2 kHz to 10 kHz band. The SAMS system is described along with deployment information and acoustic data. The time-of-flight technique is described. This method yields path-averaged sound speeds. The resulting sound speeds show little dispersion over this frequency band. An important aspect of the SAMS measurements is that they were made at the same time that the 2017 water-column acoustic measurements were made and within the band of frequencies emitted during the tows of the ITC 2015 source.

C. Short-Range Remote Sensing

Barclay *et al*. [item 14) of the Appendix] report on wideband measurements of the vertical coherence (directionality) of surface-wave-generated ambient noise. These wideband measurements from the autonomous seafloor lander "Deep Sound" were used to determine the geoacoustic properties and layer structure of the New England Mud Patch. By fitting the data with a wave number integration noise model, estimates of the compressional wave speed and attenuation in the mud layer, mud layer thickness and density, and sand layer compressional wave speed and density were obtained at three different sites. The inversion was not able to determine the shear wave speed and shear attenuation in the mud or sand layer with meaningful precision due to a lack of sensitivity of the vertical noise coherence to these geoacoustic properties.

Belcourt *et al.* [item 30) of the Appendix] applied linearized Bayesian inversion to acoustic arrival-time data for high-precision estimation of the experimental geometry at the New England Mud Patch. The ray-based inversion provided geometry estimates (required to process wide-angle reflection-coefficient data for geoacoustic inversion) to much higher precision than prior information based on GPS and bathymetry measurements.

In a second paper by Belcourt *et al.* [item 11) of the Appendix], the major results were the depth dependence of the mud geoacoustic properties and the frequency dependence of the speed of sound and attenuation along with uncertainties. The results at two sites show a nearly uniform sound speed in the mud followed by a thin transition layer in which the speed of sound rapidly increases nonlinearly. At both sites, velocity dispersion is weak, a few meters per second over the measurement band 400–1300 Hz, and attenuation follows a nearly linear frequency dependence. The results are buttressed by the consistency at two sites, as well as supporting evidence from independent measurements, cores, angle of intromission observed by Holland *et al.* [item 31) of the Appendix], and chirp-reflection data. The paper also includes comparison to the MSCL sound-speed measurements (250 kHz) conducted by Allen Reed.

Michalopoulou and Gerstoft [item 32) of the Appendix] took advantage of multipath arrivals at a set of 16 vertically separated receivers on one of the Scripps MPL VLAs. They extracted arrival times and their posterior probability densities from low frequency modulated receptions for the direct, surface-reflected, and bottom-reflected paths, as well as the reflected path from the first/second sediment layer interface. Arrival time and density estimates were computed with particle filtering. Using linearization, densities were connected to the geometry and water column sound-speed parameters, providing—in a very efficient manner entailing only a handful of iterations—point estimates as well as probability densities. These were then employed in an exhaustive search for sediment thickness and sound-speed probability density function estimation.

Potty and Miller [item 33) of the Appendix] investigated the effect of sediment shear rigidity on acoustic normal mode arrival times using data from SBCEX and Shelfbreak Primer experiments. The group speeds near the airy phase region were very sensitive to shear speeds in the bottom. Shear and compressional speeds were estimated and the results compared well with deep core data and other inversions. The inversions used modal travel times in the frequency band from 10 to 100 Hz, and the compressional wave speed in the mud layer was modeled as linearly increasing. A resolution analysis was also performed to estimate the depth resolution length in the mud layer.

D. Long-Range Remote Sensing

Bonnel *et al.* [item 34) of the Appendix] presented geoacoustic inversion results along the main track of the experiment for frequencies below 300 Hz and intermediate ranges (about 7 km). Their procedure has two steps: first the modal dispersion from single-receiver data is estimated using time warping, and second, the estimated dispersion is the input for a transdimensional Bayesian inversion algorithm. The main contribution of the paper is twofold. First, the inversion results suggest that most of the mud is effectively homogeneous followed by a transition layer with a sharp increase in sound speed, occurring above the so-called "mudbase." Second, the paper compares results for two data sets, collected independently both in time and space. Overall, the paper emphasizes the importance of extracting as much information as possible from data before inversion, and then using an adaptive inversion method to prevent overparameterization of the results.

Dahl and Dall'Osto [item 35) of the Appendix] summarized a subset of the measurements made by the Intensity Vector Autonomous Recorder (IVAR). IVAR recorded the vector acoustic field due to broadband signals originating from SUS (Mk-64) charges deployed from 3 km to 13 km distance. Four coherent channels of acoustic data were recorded continuously: one channel for acoustic pressure and three channels associated with a triaxial accelerometer from which acoustic particle velocity is obtained. Sufficient geometric dispersion at these ranges from the SUS charges permitted unambiguous identification of up to four modes as a function of frequency for frequencies less than 80 Hz. From time–frequency analysis of the dispersed arrivals, the following four quantities derived from the vector acoustic measurements were formed by coherent combination of pressure and velocity channels:

1) modal phase speed;
2) circularity, a measure of the normalized curl of active intensity;
3) depth-dependent mode speed of energy;

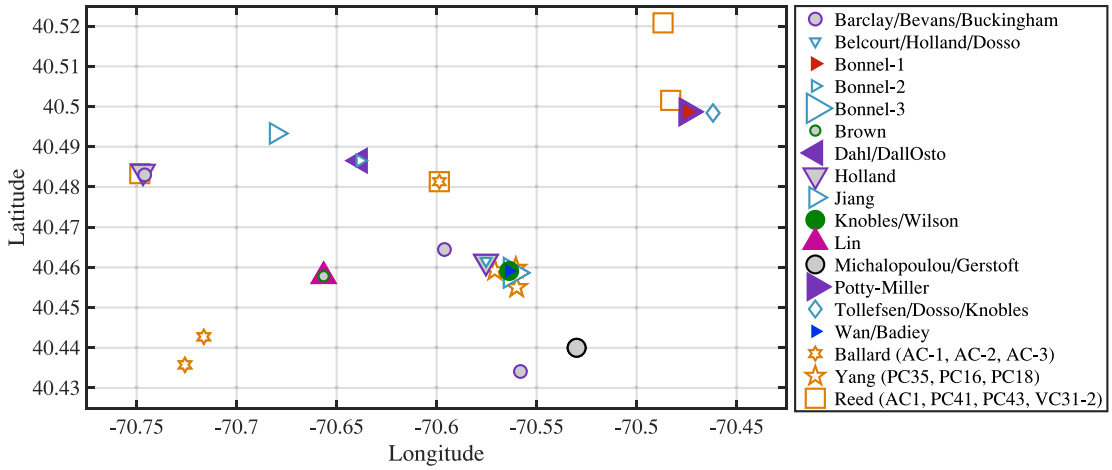

Fig. 6. Map of receiver locations used in the special issue articles. The symbols, colors, and shading are the same as in Figs. 7 and 8 and are explained in Tables IV and V.

4) vertical component of reactive intensity normalized by scalar intensity.

The last three depend on the IVAR measurement depth of 1.25 m above the seafloor.

Brown *et al.* [item 36) of the Appendix] examined the use of a physics-based model for the marine mud. Estimates for the parameters of a silt-suspension theory were found using Bayesian inference. The acoustic data were from a combustive sound source signal received on a single hydrophone. Characteristics extracted from a nearby piston core provided prior information for the physical modeling. Selection of inversion parameters was guided by both sensitivity analyses and bounds from archival and core measurements.

Knobles *et al.* [item 4) of the Appendix] discussed how a statistical inference experiment was designed using the SUS charges deployed on circles of 2-, 4-, and 6.5-km radii with the ARL:UT array in the center. The SUS measurements were viewed as data samples drawn from an ensemble of measurements taken from the same but unknown distribution. These multiple data samples allowed for *a posterior* probability distribution to be generated on each circle within the framework of a maximum entropy methodology. The propagation model used to generate hypothesis simulated time series was a finite difference range-dependent parabolic equation algorithm that was constrained by the range- and azimuth-dependent (relative to the ARL:UT array) sediment TWTT measurements by Goff [item 27) of the Appendix].

Lin *et al.* [item 37) of the Appendix] conducted numerical and experimental studies to investigate the advantage of utilizing absolute travel time information in Bayesian geoacoustic inference of broadband low-frequency acoustic data. It was shown that inversions using absolute travel time can yield smaller uncertainties compared to inversions using relative arrival time. Numerical simulations also found that absolute travel time information may have more profound advantages when the signal-to-noise ratio is low.

Tollefsen *et al.* [item 12) of the Appendix] showed that Bayesian inversion of noise due to a container ship (passing near a bottom-moored horizontal array) yielded a sound speed structure indicative of fine-grained sediment (i.e., mud) in the upper seabed and of coarse-grained sediment (i.e., sand) in the lower seabed, with a transition layer above the interface. The results were also compared to MSCL sound speed measurements (250 kHz) conducted by Reed.

Wan *et al.* [item 38) of the Appendix] focused on the low-order modes of the SUS signals from long-range and along-shelf sound propagation tracks. While a prior study [item 39) of the Appendix] used 10–80 Hz data to explore the detailed structure of the airy phase, the work reported in the special issue used 100–500 Hz, which mainly propagated in the water column and the surface fine-grained mud layer. Three modal characteristic features (i.e., modal arrival time, mode shape, and modal amplitude of low-order modes) were extracted to construct cost functions with dimension-reduced parameter space for estimation of the sound speed and attenuation of the mud layer. The effect of the uncertainty from propagation in the deep sand transition layers and half-space basement was minimized. The ambiguity of sound speed at the top of the mud layer and sound-speed gradient in the mud (discussed in item 39) of the Appendix) was successfully removed using a two-stage inversion process, including mode-shape-based inversion and modal-dispersion-based inversion.

V. Comparison of Results

In this section, we collect SBCEX results reported independently in the papers that appear in this special issue, along with four SBCEX results that have been reported elsewhere [items 31) and 39)–41) of the Appendix]. Estimates of the sound-speed ratio (SSR) (the sound speed at the top of the sediment normalized by the contemporaneous sound speed of the bottom water) at the sites shown in Fig. 6 are collected in Fig. 7. These surface SSR estimates result from one of three assumptions about the depth dependence of the sound speed in the sediment, indicated by the face color of the symbols. To explicitly take into account the depth averaging associated with each result,

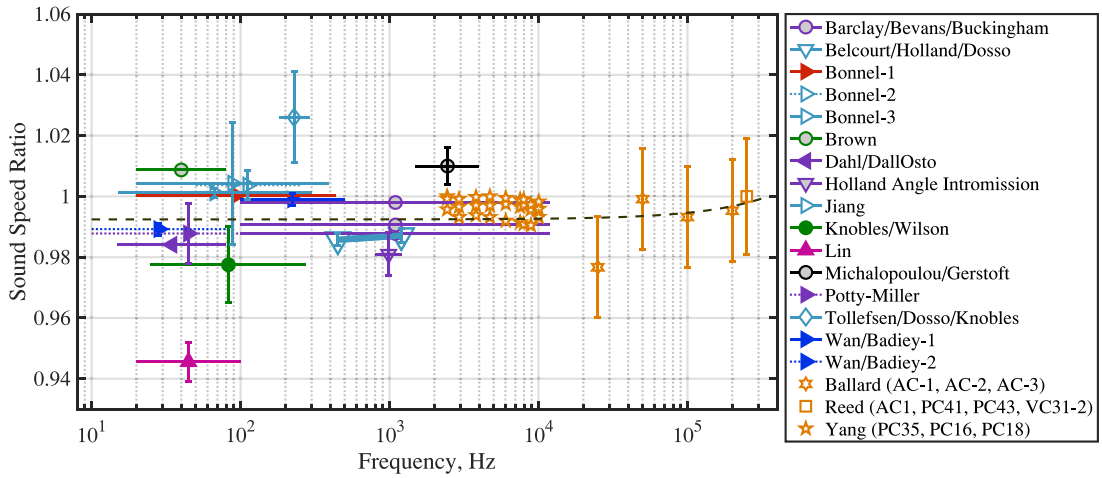

Fig. 7. SSRs (sound speeds normalized by the associated bottom water sound speeds), for the surface sediment layer, obtained from remote sensing (details provided in Tables IV and V) and direct measurements (orange) are shown. Single data points with horizontal bars appear at the geometric mean frequency of the associated analysis band. The thick line connecting the two inverted-triangle symbols indicate the dispersion obtained from narrowband inversions over that frequency range. Yang's results show the three uppermost depth estimates at each frequency from SAMS deployments near the three core locations shown in the legend [item 10) of the Appendix]. Ballard's results are the mean sound speeds of the three cores shown in the legend, after first depth averaging over the upper 50 cm [item 9) of the Appendix]. The vertical bars show measurement uncertainty calculated from a propagation of error analysis, accounting for timing and positioning uncertainty. Reed's 250-kHz core logger result is the mean sound speed from the four cores shown in the legend, after first depth averaging all the measurements from each core [item 9), 11), and 12) of the Appendix]. The error bars represent ± 1 standard deviation of the spatial variability. The dashed line shows a linear fit to the SSR results: $\mathrm{SSR}_{\mathrm{fit}} = 0.9924 + (2.164 \times 10^{-8})f$, as described in the text.

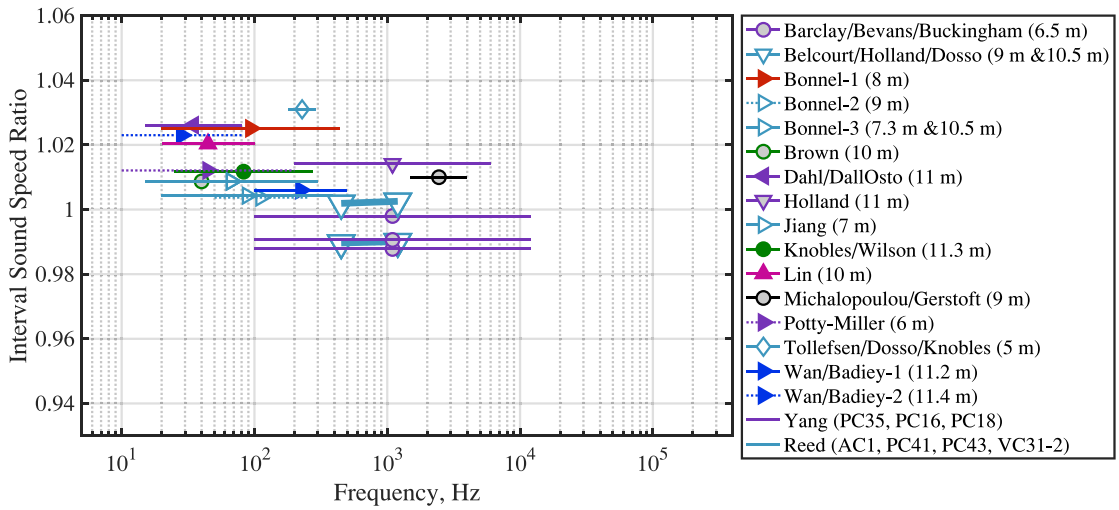

Fig. 8. To help illustrate the various upper layer sound-speed gradient results, interval SSRs inferred from short- and long-range remote sensing, over the sediment thicknesses shown in parentheses, are shown. Details of the symbols and colors are provided in Tables IV and V, respectively. Single data points with horizontal bars appear at the geometric mean frequency of the associated analysis band. The thick lines connecting two symbols indicate the dispersion obtained from narrowband inversions over that frequency range. In the cases where two depths are shown in the legend, results for two different depth integrations are shown. The shallower depth in all cases corresponds to the lower interval sound-speed value.

the interval SSRs are presented in Fig. 8. For each result in Figs. 7 and 8, the horizontal spread indicates the frequency band used, and the vertical bars in Fig. 7 indicate the reported uncertainty or variability. Symbols indicate the type of data used in each study, and colors indicate the analysis or inference method; complete descriptions of the markers and colors used in these figures are provided in Tables IV and V. The types of input data and the acoustic sources are listed in Table IV, and the receiver arrays and inference methods used are given in Table V.

Unlike the SAX experiments that showed a significant degree of dispersion for a sand sediment [item 20) of the Appendix], the composite measurements and inferences of the surface SSR for the central mud patch (see Fig. 7) show relatively little dispersion. With a few exceptions, the SSR values lie between 0.98 and 1.01 over the 10 kHz to 250 kHz band. Using the reported SSR at the geometric mean of each frequency band, a linear curve fit yields $\mathrm{SSR}_{\mathrm{fit}} = 0.9924 + (2.164 \times 10^{-8})f$, shown as the dashed line in Fig. 7. When the reported uncertainties and variation are considered, there is a significant

TABLE IV
MARKERS USED ON SOUND-SPEED PLOTS CORRESPOND TO THE TYPE OF INPUT DATA

	Input Data / Groups	**Sound source**
○	**Pressure time series**	
	Barclay *et al.* [item 14) in the Appendix]	ambient noise
	Brown *et al.* [item 36) in the Appendix]	ARL:UT CSS
	Knobles *et al.* [item 4) in the Appendix]	**SUS circles**
	Michalopoulou/Gerstoft [item 32) in the Appendix]	MPL LFM
▷	**Modal properties**	
	Bonnel-1 [item 41) in the Appendix]	ARL:UT CSS
	Bonnel-2 [item 34) in the Appendix]	APL-UW J15
	Bonnel-3 [item 34) in the Appendix]	ARL:UT CSS
	Jiang *et al.* [item 40) in the Appendix]	ARL:UT CSS
	Potty/Miller [item 33) in the Appendix]	SUS
	Wan/Badiey-1 [item 38) in the Appendix]	**Long-range SUS**
	Wan/Badiey-2 [item 39) in the Appendix]	Long-range SUS
◁	**Vector intensity**	
	Dahl/Dall'Osto [item 35) in the Appendix]	**SUS**
▽	**Reflection coefficients**	
	Belcourt *et al.* [item 11) in the Appendix]	AA201
	Holland *et al.* [item 31) in the Appendix]	AA201
△	**Absolute travel time**	
	Lin *et al.* [item 37) in the Appendix]	ARL:UT CSS
◇	**Spectrograms**	
	Tollefsen *et al.* [item 12) in the Appendix]	ship noise

The acoustic source is also listed, with **Bold** indicating results that use multiple source locations.

TABLE V
COLORS ON SOUND-SPEED PLOTS CORRESPOND WITH THE TYPE OF INFERENCE METHOD

Color	**Method** / Groups	**Receiver array**
Green	**Max.Ent. Bayesian**	
	Brown *et al.* [item 36) in the Appendix]	SHRU912
	Knobles *et al.* [item 4) in the Appendix]	ARL:UT L array
Light Blue	**Trans-D Bayesian**	
	Belcourt *et al.* [item 11) in the Appendix]	ARL:PSU RHS
	Bonnel-2 [item 34) in the Appendix]	APL-UW IVAR
	Bonnel-3 [item 34) in the Appendix]	ARL:UT L array
	Jiang *et al.* [item 40) in the Appendix]	ARL:UT L array
	Tollefsen *et al.* [item 12) in the Appendix]	FFI HLA
Black	**Particle Filtering**	
	Michalopoulou/Gerstoft [item 32) in the Appendix]	MPL VLA2
Purple	**By Observation**	
	Barclay *et al.* [item 14) in the Appendix]	Deep Sound Source
	Dahl/Dall'Osto [item 35) in the Appendix]	APL-UW IVAR
	Holland *et al.* [item 31) in the Appendix]	ARL:PSU RHS
	Potty/Miller [item 33) in the Appendix]	URI Sled
Bright Blue	**Empirical with Airy phase**	
	Wan/Badiey-1 [item 38) in the Appendix]	ARL:UT L array
	Wan/Badiey-2 [item 39) in the Appendix]	ARL:UT L array
Red	**Least-squares**	
	Bonnel-1 [item 41) in the Appendix]	URI Geosled
Pink	**Bayesian**	
	Lin *et al.* [item 37) in the Appendix]	WHOI SHRU

On the plot, color-filled symbols assumed linear sound-speed gradient and gray-filled symbols assumed no gradient, and open symbols had no assumption about gradient.

overlap among the results. However, the variability of statistical inference methods, prior assumptions about the seabed geoacoustic parameterization, the information content in the input data, and spatial variability of the physical characteristics of the fine-grained sediment could possibly explain the degree of variability seen in Fig. 7. The physical variability is supported by Barclay *et al.*'s [item 14) of the Appendix] results for multiple locations that show a spread of about ± 0.02 in the SSR values.

Some of the variability in the surface SSRs (see Fig. 7) can be ascribed to differences in the assumed or inferred depth dependence of the sediment sound speed. These differences are partially accounted for by looking at the interval sound speed for each of the remote sensing results, as shown in Fig. 8. The interval sound speeds are calculated over the inferred thickness of the top layer (listed in the legend). Results based on the assumption that the sound speed was constant in the sediment layer are filled with gray; these have the same surface and interval SSRs. Others (open symbols) allowed the inversion methods to determine the depth dependence, such as in the transdimensional Bayesian inversion algorithm. Some of the transdimensional Bayesian results show an isospeed mud down to about 3 m above the mud base followed by a transition layer in which there is a rapid increase in the sound speed. To show the impact of this rapid increase, the interval sound speed is calculated using two depths for two of these cases [see items 11) and 34) of the Appendix]. In both cases, the larger depth, which includes the transition layer, leads to a greater interval sound speed. The remaining results (filled, single-color symbols) were based on the assumption that the sediment sound speed increased linearly with depth to mitigate the number of search parameters. Some of these studies found a significant gradient; others found only a small gradient. The studies reporting a large gradient, such as Lin *et al.* [item 37) of the Appendix], have higher interval SSRs than surface SSRs. These results demonstrate the ambiguity between surface sound speed and the sound-speed gradient, which is also depicted in Fig. 6 of item 38) of the Appendix. Thus, the ability to make a definitive statement on the depth dependence and dispersion of the mud sediment will require additional analysis.

A final point regarding the comparison of results collected at different times is worth noting. There is evidence that both temperature [item 42) of the Appendix] and salinity [item 43) of the Appendix] diffusion can dynamically affect the acoustic properties of fine-grained sediments. In these cases, the normalization of sediment sound speed by the bottom water sound speed alone may not yield appropriate comparisons. Knowledge of both the history of the bottom water conditions and the diffusion coefficients is required. None of the papers in this special issue have addressed this effect and it is beyond the scope of this overview to quantify it. Instead, we point out that the subbottom profile data were collected in July 2015 [item 27) of the Appendix], the ASC [item 9) of the Appendix], and

MSCL [items 9), 11), and 12) of the Appendix] measurements were collected during the 2016 survey cruise, which occurred in late April, and all the other measurements reported in this collection were from early March to early April 2017.

VI. Conclusion

A broad overview of the field work conducted during the SBCEX has been provided. SBCEX included a comprehensive subbottom chirp profile of the experimental area, about 200 sediment cores, and a number of direct *in situ* measurements of the acoustic properties of the seabed. Numerous acoustic propagation measurements throughout the experimental site provided data for inversion processes and statistical inference techniques to remotely sense the acoustic properties of the bottom. The scientific plan of these measurements and the supporting oceanographic and environmental measurements allowed the various principal investigators to begin to achieve the goals outlined in the introduction of this editorial, and thereby increase the community's understanding of the acoustic properties of the fine-grained sediment at the site.

Analysis associated with SBCEX is ongoing and a second volume of this special issue is planned. Some of the topics that still need to be investigated include the following:

1) a more complete documentation of the physical analysis of the sediment core material by USGS;
2) additional sound-speed and new attenuation results including study of dispersion;
3) more model data comparison for both sediment acoustic properties and for the acoustic field in the water column;
4) more analysis on uncertainty and variability of both the acoustic field and sediment properties.

Acknowledgment

The guest editors would like to thank the U.S. Navy Office of Naval Research for its support and the Ocean Acoustics program officers, D. Reeder, K. Becker, R. Headrick, and R. Soukup, for their guidance. The authors also acknowledge and thank all the SBCEX participants, including the captains and crews of *RV Neil Armstrong, RV Endeavor,* and *RV Sharp.*

Preston S. Wilson, *Guest Editor*
Walker Department of
Mechanical Engineering
and Applied Research Laboratories
The University of Texas at Austin
Austin, TX 78713 USA

David P. Knobles, *Guest Editor*
Knobles Scientific and Analysis
Austin, TX 78713 USA

Tracianne B. Neilsen, *Guest Editor*
Department of Physics and Astronomy
Brigham Young University
Provo, UT 84602 USA

Appendix
Related Work

1) N. P. Chotiros, *Acoustics of the Seabed as a Poroelastic Medium*. Berlin, Germany: Springer, 2017.
2) J. F. Lynch, S. R. Ramp, C.-S. Chiu, T. Y. Tang, Y. Yang, and J. A. Simmen, "Research highlights from the Asian Seas International Acoustics Experiment in the South China Sea," *IEEE J. Ocean. Eng.*, vol. 29, no. 4, pp. 1067–1074, Oct. 2004.
3) P. H. Dahl *et al.*, "Overview of results from the Asian Seas International Acoustics Experiment in the East China Sea," *IEEE J. Ocean. Eng.*, vol. 29, no. 4, pp. 920–928, Oct. 2004.
4) D. P. Knobles *et al.*, "Maximum entropy derived statistics of sound-speed structure in a fine-grained sediment inferred from sparse broadband acoustic measurements on the New England continental shelf," *IEEE J. Ocean. Eng.*, vol. 45, no. 1, pp. 161–173, Jan. 2020, doi: 10.1109/JOE.2019.2922717.
5) C. K. Wentworth, "A scale of grade and class terms for clastic sediments," *J. Geol.*, vol. 30, no. 5, pp. 377–392, 1922.
6) W. C. Krumbein, "Size frequency distributions of sediments," *J. Sedimentary Res.*, vol. 4, no. 2, pp. 65–77, 1934.
7) J. H. Miller, L. R. Bartek, G. R. Potty, D. Tang, J Na, and Y. Qi, "Sediments in the East China Sea," *IEEE J. Ocean. Eng.*, vol. 29, no. 4, pp. 940–951, Oct. 2004.
8) G. R. Potty and J. H. Miller, "Inversion of sediment parameters in the Biot parameter space," *Proc. Meetings Acoust.*, vol. 22, no. 1, 2014, Art no. 070004.
9) M. S. Ballard *et al.*, "*In situ* measurements of compressional wave speed during gravity coring operations in the New England Mud Patch," *IEEE J. Ocean. Eng.*, vol. 45, no. 1, pp. 26–38, Jan. 2020, doi: 10.1109/JOE.2019.2924560.
10) J. Yang and D. Jackson, "Measurement of sound speed in fine-grained sediments during the Seabed Characterization Experiment," *IEEE J. Ocean. Eng.*, vol. 45, no. 1, pp. 39–50, Jan. 2020, doi: 10.1109/JOE.2019.2946004.
11) J. Belcourt, C. W. Holland, S. E. Dosso, J. Dettmer, and J. A. Goff, "Depth-dependent geoacoustic inferences with dispersion at the New England Mud Patch via reflection coefficient inversion," *IEEE J. Ocean. Eng.*, vol. 45, no. 1, pp. 69–91, Jan. 2020, doi: 10.1109/JOE.2019.2900115.
12) D. Tollefsen, S. E. Dosso, and D. P. Knobles, "Ship-of-opportunity noise inversions for geoacoustic profiles of a layered mud-sand seabed," *IEEE J. Ocean. Eng.*, vol. 45, no. 1, pp. 189–200, Jan. 2020, doi: 10.1109/JOE.2019.2908026.
13) P. S. Wilson, D. P. Knobles, P. H. Dahl, A. R. McNeese, and M. C. Zeh, "Short-range signatures of explosive sounds in shallow water used for seabed characterization," *IEEE J. Ocean. Eng.*, vol. 45, no. 1, pp. 14–25, Jan. 2020, doi: 10.1109/JOE.2019.2934372.

14) D. R. Barclay, D. A. Bevans, and M. J. Buckingham, "Estimation of the geoacoustic properties of the New England Mud Patch from the vertical coherence of the ambient noise in the water column," *IEEE J. Ocean. Eng.*, vol. 45, no. 1, pp. 51–59, Jan. 2020, doi: 10.1109/JOE.2019.2932651.
15) E. I. Thorsos, M. D. Richardson, and J. F. Lynch, "Guest Editorial Special Issue on Sediment Acoustic Processes," *IEEE J. Ocean. Eng.*, vol. 33, no. 4, pp. 357–358, Oct. 2008.
16) E. I. Thorsos, M. D. Richardson, and J. F. Lynch, "Guest Editorial Special Issue on Sediment Acoustic Processes: Part II," *IEEE J. Ocean. Eng.*, vol. 34, no. 4, pp. 369–371, Oct. 2009.
17) E. I. Thorsos, M. D. Richardson, and J. F. Lynch, "Guest Editorial Special Issue on Sediment Acoustic Processes: Part III," *IEEE J. Ocean. Eng.*, vol. 35, no. 3, pp. 449–452, Jul. 2010.
18) M. D. Richardson *et al.*, "Overview of SAX99: Environmental considerations," *IEEE J. Ocean. Eng.*, vol. 26, no. 1, pp. 26–53, Jan. 2001.
19) A. H. Reed, K. E. Thompson, K. B. Briggs, and C. S. Willson, "Physical pore properties and grain interactions of SAX04 sands," *IEEE J. Ocean. Eng.*, vol. 35, no. 3, pp. 488–501, Jul. 2010.
20) K. L. Williams, D. R. Jackson, E. I. Thorsos, D. Tang, and S. G. Schock, "Comparison of sound speed and attenuation measured in a sandy sediment to predictions based on the Biot theory of porous media," *IEEE J. Ocean. Eng.*, vol. 27, no. 3, pp. 413–428, Jul. 2002.
21) M. A. Zimmer, L. D. Bibee, and M. D. Richardson, "Measurement of the frequency dependence of the sound speed and attenuation of seafloor sands from 1 to 400 kHz," *IEEE J. Ocean. Eng.*, vol. 35, no. 3, pp. 538–557, Jul. 2010.
22) D. Tang *et al.*, "Shallow Water '06: A joint acoustic propagation/nonlinear internal wave physics experiment," *Oceanography*, vol. 20, pp. 156–167, Dec. 2007.
23) J. Lynch and D. Tang, "Overview of Shallow Water 2006 *JASA EL* special issue papers," *J. Acoust. Soc. Amer.*, vol. 124, no. 3, pp. EL63–EL65, 2008.
24) N. R. Chapman and J. F. Lynch, "Editorial: Special Issue on the 2006 Shallow Water Experiment," *IEEE J. Ocean. Eng.*, vol. 35, no. 1, pp. 1–2, Jan. 2010.
25) N. R. Chapman and J. F. Lynch, "Editorial: Special Issue on the 2006 Shallow Water Experiment (Part II)," *IEEE J. Ocean. Eng.*, vol. 35, no. 4, pp. 682–683, Oct. 2010.
26) J. A. Goff *et al.*, "Seabed characterization on the New Jersey middle and outer shelf: Correlatability and spatial variability of seafloor sediment properties," *Mar. Geol.*, vol. 209, no. 1, pp. 147–172, 2004.
27) J. A. Goff, A. H. Reed, G. Gawarkiewicz, P. S. Wilson, and D. P. Knobles, "Stratigraphic analysis of a sediment pond within the New England Mud Patch: New constraints from high-resolution chirp acoustic reflection data," *Mar. Geol.*, vol. 412, pp. 81–94, 2019.
28) C. de Moustier, "Oceanographic constraints on seafloor surveys of the New England continental shelf," *J. Acoust. Soc. Amer.*, vol. 139, no. 4, 2016, Art. no. 2111.
29) J. A. Goff, "Modern and fossil pockmarks in the New England Mud Patch: Implications for submarine groundwater discharge on the middle shelf," *Geophys. Res. Lett.*, vol. 46, no. 21, pp. 12213–12220, 2019.
30) J. Belcourt, S. E. Dosso, C. W. Holland, and J. Dettmer, "Linearized Bayesian inversion for experiment geometry at the New England Mud Patch," *IEEE J. Ocean. Eng.*, vol. 45, no. 1, pp. 60–68, Jan. 2020, doi: 10.1109/JOE.2019.2900194.
31) C. Holland, J. Belcourt, and S. E. Dosso, "Geoacoustic inferences from seabed reflection measurements on the New England Mud Patch," *J. Acoust. Soc. Amer*, vol. 142, 2017, Art. no. 2590.
32) Z. Michalopoulou and P. Gerstoft, "Multipath broadband localization, bathymetry, and sediment inversion," *IEEE J. Ocean. Eng.*, vol. 45, no. 1, pp. 92–102, Jan. 2020, doi: 10.1109/JOE.2019.2896681.
33) G. R. Potty and J. H. Miller, "Effect of shear on modal arrival times," *IEEE J. Ocean. Eng.*, vol. 45, no. 1, pp. 103–115, Jan. 2020, doi: 10.1109/JOE.2019.2925920.
34) J. Bonnel, S. E. Dosso, D. Eleftherakis, and N. R. Chapman, "Trans-dimensional inversion of modal dispersion data on the New England Mud Patch," *IEEE J. Ocean. Eng.*, vol. 45, no. 1, pp. 116–130, Jan. 2020, doi: 10.1109/JOE.2019.2896389.
35) P. H. Dahl and D. R. Dall'Osto, "Vector acoustic analysis of time-separated modal arrivals from explosive sound sources during the 2017 Seabed Characterization Experiment," *IEEE J. Ocean. Eng.*, vol. 45, no. 1, pp. 131–143, Jan. 2020, doi: 10.1109/JOE.2019.2902500.
36) E. M. Brown, Y. Lin, J. D. Chaytor, and W. L. Siegmann, "Geoacoustic inversion for a New England Mud Patch sediment using the silt-suspension theory of marine mud," *IEEE J. Ocean. Eng.*, vol. 45, no. 1, pp. 144–160, Jan. 2020, doi: 10.1109/JOE.2019.2934604.
37) Y. Lin, J. Bonnel, D. P. Knobles, and P. S. Wilson, "Broadband waveform geoacoustic inversions with absolute travel time," *IEEE J. Ocean. Eng.*, vol. 45, no. 1, pp. 174–188, Jan. 2020, doi: 10.1109/JOE.2019.2919859.
38) L. Wan, M. Badiey, D. P. Knobles, P. S. Wilson, and J. A. Goff, "Estimates of low-frequency sound speed and attenuation in a surface mud layer using low-order modes," *IEEE J. Ocean. Eng.*, vol. 45, no. 1, pp. 201–211, Jan. 2020, doi: 10.1109/JOE.2019.2923861.
39) L. Wan, M. Badiey, D. P. Knobles, and P. S. Wilson, "The Airy phase of explosive sounds in shallow water," *J. Acoust. Soc. Amer.*, vol. 143, no. 3, pp. EL199–EL205, 2018.
40) Y.-M. Jiang, S. E. Dosso, and C. W. Holland, "Seabed geoacoustic inversion using a hydrophone equipped underwater glider," *J. Acoust. Soc. Amer.*, vol. 144, no. 3, 2018, Art. no. 1972.

41) J. Bonnel *et al.*, "Geoacoustic inversion on the New England Mud Patch using warping and dispersion curves of high-order modes," *J. Acoust. Soc. Amer.*, vol. 143, no. 5, pp. EL405–EL411, 2018.
42) W. T. Wood, K. M. Martin, W. Jung, and J. Sample, "Seismic reflectivity effects from seasonal seafloor temperature variation," *Geophys. Res. Lett.*, vol. 41, no. 19, pp. 6826–6832, 2014.
43) G. R. Venegas, J. D. Sagers, and P. S. Wilson, "Laboratory measurements and simulations of reflections from a water/clay interface during the diffusion of salt," *J. Acoust. Soc. Amer.*, vol. 146, no. 2, pp. 1384–1393, 2019.

Preston S. Wilson received the B.S.M.E. and M.S.M.E. degrees from The University of Texas at Austin, Austin, TX, USA, in 1990 and 1994, respectively, and the Ph.D. degree in mechanical engineering from Boston University, Boston, MA, USA, in 2001.

He is currently a Professor and Raymond F. Dawson Centennial Fellow in engineering with the University of Texas at Austin, with joint appointments in the Mechanical Engineering Department and at Applied Research Laboratories (ARL:UT). He was a Research Engineer with ARL:UT from 1993 to 1997 and a Postdoctoral Fellow with Boston University from 2001 to 2003. He has been a faculty member with The University of Texas at Austin since 2003. He is a cofounder of AdBm, Inc., operating in the underwater noise mitigation arena. He is currently the Co-Chief Scientist for the ONR Seabed Characterization Experiment. His work has been reported in more than 360 peer-reviewed papers, conference proceedings, technical reports, and published presentation abstracts. He holds six U.S. patents. His research interests include physical acoustics, underwater acoustics, engineering acoustics, and bioacoustics, with specific areas of interests in sound propagation in shallow water, in water-saturated sediments, bubbly liquid, and multiphase material.

Dr. Wilson is a Fellow of the Acoustical Society of America (ASA), the past Chair of the Committee for Education in Acoustics of the ASA, and a Member of the Executive Council of the ASA. He is an Associate Editor for the *Journal of the Acoustical Society of America*. He was the recipient of the A.B. Wood Medal from the Institute of Acoustics U.K.

David P. Knobles received the Ph.D. degree in nuclear physics in 1989 from The University of Texas at Austin, Austin, TX, USA.

From 1989 to 1992, he was a Postdoctoral Fellow in nuclear theory with The University of Texas at Austin. He is the owner of Knobles Scientific and Analysis, a private business that specializes in defense and environmental applications. He has been a Principle Investigator in the Ocean Acoustics Program at the Office of Naval Research since 2002. He taught graduate courses with The University of Texas at Austin in methods of mathematical physics and ocean acoustics. He is currently the Co-Chief Scientist for the ONR Seabed Characterization Experiment. His research interests include the quantum many-body problem, remote sensing, cosmology, and bioacoustics.

Dr. Knobles is a Fellow of the Acoustical Society of America.

Tracianne B. Neilsen received the Ph.D. degree in physics from The University of Texas at Austin, Austin, TX, USA, in 2000.

Her postdoctoral research was completed at the Applied Research Laboratories, The University of Texas at Austin, investigating iterative optimizations for source localization and seabed parameterization in shallow ocean environments. Working as a part-time Research Scientist though 2007, her focus shifted to optimizations for high-frequency seabed parameterization using the Biot model. For more than a decade, she was a part-time Assistant Professor with Brigham Young University, Provo, UT, USA, and did research on jet noise source characterization. In May 2018, she became a full-time Professor and returned to underwater acoustics research. She has recently been exploring effective ways to apply deep learning in ocean acoustics. She is currently an Associate Professor with the Department of Physics and Astronomy, Brigham Young University.